



**HAL**  
open science

# High resolution upper mantle discontinuity images across the Pacific Ocean from SS precursors using local slant stack filters

Zhao Zheng, Sergi Ventosa, Barbara Romanowicz

► **To cite this version:**

Zhao Zheng, Sergi Ventosa, Barbara Romanowicz. High resolution upper mantle discontinuity images across the Pacific Ocean from SS precursors using local slant stack filters. *Geophysical Journal International*, 2015, 202 (1), pp.175 - 189. 10.1093/gji/ggv118 . insu-01400574

**HAL Id: insu-01400574**

**<https://insu.hal.science/insu-01400574>**

Submitted on 22 Nov 2016

**HAL** is a multi-disciplinary open access archive for the deposit and dissemination of scientific research documents, whether they are published or not. The documents may come from teaching and research institutions in France or abroad, or from public or private research centers.

L'archive ouverte pluridisciplinaire **HAL**, est destinée au dépôt et à la diffusion de documents scientifiques de niveau recherche, publiés ou non, émanant des établissements d'enseignement et de recherche français ou étrangers, des laboratoires publics ou privés.

# High resolution upper mantle discontinuity images across the Pacific Ocean from *SS* precursors using local slant stack filters

Zhao Zheng,<sup>1,\*</sup> Sergi Ventosa<sup>2</sup> and Barbara Romanowicz<sup>1,2,3</sup>

<sup>1</sup>*Berkeley Seismological Laboratory, University of California, Berkeley, CA, USA. E-mail: zhaozheng@berkeley.edu*

<sup>2</sup>*Institut de Physique du Globe, Paris, France*

<sup>3</sup>*Collège de France, Paris, France*

Accepted 2015 March 10. Received 2015 February 5; in original form 2014 September 4

## SUMMARY

*SS* precursor observations are a powerful tool to study the topography and character of transition zone discontinuities, especially in regions such as ocean basins where few seismic stations exist, precluding other high resolution approaches. Still, the available coverage is limited by the distribution of sources and stations, but also by the level of noise and by the fact that, in some distance ranges, interfering seismic phases mask the weak signal from the *SS* precursors. We introduce an array data processing tool, the local slant-stack filter, to address these challenges and clean up the otherwise noisy *SS* precursor record sections. We show that these filters are a powerful tool for extracting the weak yet coherent *SS* precursor signals while removing interfering seismic phases as well as random noise, yielding robust precursor traveltimes measurements with spatial resolution higher than what can be achieved by the conventional common midpoint stacking method. The effectiveness of the filters are demonstrated by application to synthetic and real data. We systematically apply this filtering method to an *SS* precursor data set recorded by the U.S. Transportable Array that samples a vast region of the Pacific Ocean and its northwest margin, and present maps of 410 and 660 discontinuity topography. We discuss correlations observed between our discontinuity images and several fine-scale heterogeneities revealed by mantle shear wave tomography in the vicinity of Hawaii and the Pacific Superswell.

**Key words:** Image processing; Body waves; Wave scattering and diffraction.

## 1 INTRODUCTION

Two seismic discontinuities, at approximate depths of 410 and 660 km, are globally present in the Earth's upper mantle and are featured in 1-D reference models such as *PREM* (Dziewonski & Anderson 1981). It is generally agreed that these two discontinuities are caused by phase transitions of mantle minerals, in particular from olivine to wadsleyite at ~410 km and from ringwoodite to perovskite + magnesiowüstite at ~670 km (Ringwood 1975; Ito & Takahashi 1989; Ita & Stixrude 1992). In addition to olivine, other minor minerals such as garnet also play a role (Vacher *et al.* 1998). The depth (or pressure) at which these phase transitions occur is a function of temperature and composition, therefore topography of the 410 and 660 discontinuities can serve as a proxy for the detection of thermal and chemical heterogeneities in that part of the mantle (Bina & Helffrich 1994; Stixrude 1997; Helffrich 2000; Shearer 2000). The Clapeyron slopes of the olivine transitions predict a deepened '410' and a shallower '660' in the presence of a hot

anomaly (e.g. mantle plume) and the opposite for a cold anomaly (e.g. subducted slab). Such correlations have been reported in certain locations of the earth particularly near subduction zones (Fukao *et al.* 2009), but the relationship is not as straightforward as would be expected for a simple thermal effect.

The topography of these discontinuities should provide important constraints on the temperature, composition and dynamics of the mantle. To image these discontinuities, one particularly useful data type is that of *SS* precursors (e.g. Shearer 1991). These are the underside reflections off the upper mantle discontinuities (Fig. 1). Since the ray paths of a precursor and the *SS* main phase are nearly identical outside the bounce point region, one can measure the differential traveltimes between the two phases and translate that to the depth of the associated discontinuity at the bounce point, for an assumed crust and upper mantle velocity structure. A major advantage of the *SS* precursors, compared to the other data types such as receiver function and triplication, is that they are sensitive to the structure at the midpoint between the seismic source and the receiver, therefore providing good coverage for the vast oceanic areas where very few seismic stations are deployed. Pioneered by Shearer (1991), in the past two decades, there have been quite a few studies which utilize *SS* precursors to produce global maps of

\*Now at: Pinnacle – A Halliburton Service, 9949 W Sam Houston Pkwy N, Houston, TX 77064, USA.

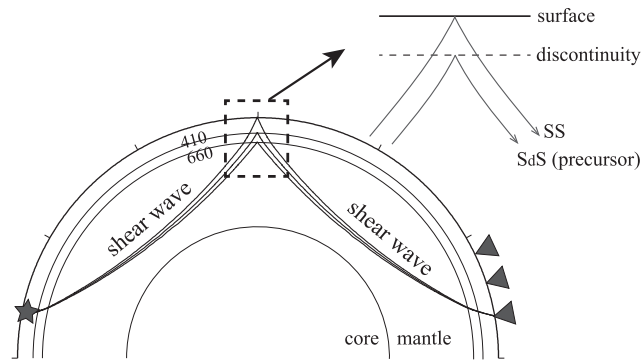


**Figure 1.** The ray paths of *SS* and its precursors. The *SS* precursors are shear waves reflected off the bottom side of the discontinuities (e.g. the 410 and the 660) in the Earth's upper mantle.

410 and 660 topography and transition zone thickness (e.g. Flanagan & Shearer 1998; Deuss & Woodhouse 2002; Gu & Dziewonski 2002; Houser *et al.* 2008; Lawrence & Shearer 2008). These maps generally agree on very long wavelength features, although considerable discrepancies exist on smaller scales (for a review, see Deuss 2009). On the regional scale, the precursor method has also been applied in a few locations where dense array coverage is available. Such regions include the central Pacific around Hawaii (Schmerr & Garnero 2006; Cao *et al.* 2010; Cao *et al.* 2011), south America (Schmerr & Garnero 2007; Contenti *et al.* 2012), eastern Asia (Heit *et al.* 2010), Japan and Kurile (Schmerr & Thomas 2011) and the northwestern Pacific (Gu *et al.* 2012).

In recent years, the resolution of global mantle tomography has been steadily improving, and the most recent global shear wave models (e.g. Debayle & Ricard 2012; French *et al.* 2013; Schaeffer & Lebedev 2013) are capable of resolving heterogeneities on the scale of a few hundred kilometres. In parallel, there has been an increasing demand for higher resolution images of mantle discontinuities topography, in order to examine the degree of correlation between the two, if any. However, the spatial resolution of the discontinuity images retrieved from the *SS* precursors has been limited due to several factors. First of all, the precursors are weak in amplitude (typically <10 per cent of the *SS* main phase), often at or below noise level. Therefore it is usually impossible to identify the precursors or make traveltimes measurements from single seismograms, and stacking is necessary. In practice, common-midpoint (CMP) stacking over rather large geographic bins (radii of 10° or 5°) are used (for a review, see Deuss 2009), which limits the spatial resolution. Secondly, the *SS* precursors suffer from interference with other seismic phases, such as the postcursors of  $S_{\text{diff}}$  (or *S* at shorter distances) and the precursors to  $S_cSScS$ . To avoid the interferences, generally, past studies have limited the epicentral distance of data selection to the 'safe ranges' [e.g. Schmerr (2012) uses 95–115° and 140–145°], although theoretically, the *SS* precursors exist over the entire range of 80–160°. This has reduced the amount of available data by a significant fraction and may have degraded the sampling density and led to the loss of spatial resolution.

To improve the spatial resolution of the discontinuity images, both dense array data and improved imaging methods are required. Data wise, the deployment of the dense and broad U.S. Transportable Array (TA) this past decade have provided an unprecedented opportunity. The large volume high quality data that TA produced have been widely utilized by numerous studies in various aspects of seismology. As a rule of thumb, the station spacing of TA is ~70 km, so the spacing between *SS* bounce points is half of that, that

is ~35 km. This presumably allows for much higher spatial resolution than what was achieved by past *SS* precursor studies using data from the global seismic network. On the other hand, in terms of method, migration was attempted as early as Shearer *et al.* (1999), but not very successfully, probably due to the poorer data density available at the time. Recently, several studies (e.g. Thomas & Billen 2009; Schmerr & Thomas 2011; Schmerr *et al.* 2013) have successfully applied migration to much denser array data in a few local/regional cases. Due to high computational cost, a 1-D model is often assumed in migration, which is a limiting factor. Cao *et al.* (2010, 2011) introduced the Generalized Radon Transform method, which seeks to exploit the very noisy coda of *SS* precursors to account for non-specular (second-order) reflections from the discontinuities. Very recently, Kim & Lawrence (2013) have developed an adaptive CMP stacking scheme by allowing flexible stacking bin size according to data density. In this paper, we propose a new array processing method called the local slant-stack filters (LSSFs). It originates from exploration seismology, and is specifically designed for the purpose of extracting weak but coherent signals from a seismic record section, while removing interfering phases as well as random noise, thus a very suitable tool for the *SS* precursor studies. In the following sections, we will first introduce the method, and test it with synthetic and real data, and then present results of application to an *SS* precursor data set recorded by the TA that samples the Pacific Ocean.

## 2 METHOD

### 2.1 The LSSF

Slowness slant stacking (also delay-and-sum or stacking) is a commonly used tool in seismic array processing. It stacks all traces in a record section along various slownesses in order to find an optimal slowness that maximizes the stacked amplitude (or other measures of signal coherence). The stacked amplitude versus slowness plot is known as a 'vespagram'. The local slant-stack transform (LSST, Ottolini 1983; Harlan *et al.* 1984; Bohlen *et al.* 2004; Shlivinski *et al.* 2005) is an extension of the above-mentioned simple stacking scheme. As the name suggests, it is a localized version of slant stacking. Fig. 2 shows an example from an exploration seismology setting, and the theory is briefly described below. Following Ventosa *et al.* (2012), the LSST of a seismic record section  $u(x, t)$  is defined as:

$$v(\eta, \tau; p) = \int_{-\infty}^{+\infty} g(x - \eta)u[x, \tau + p(x - \eta)] dx, \quad (1)$$

where  $\tau$  and  $\eta$  denote the time delay and spatial offset in the transformed domain, respectively;  $p$  is the slowness, and  $g(x)$  a spatial windowing or weighting function. In the discrete form, the LSST is defined as:

$$v_{s,m}[n] = \sum_{i=-\frac{L-1}{2}}^{\frac{L-1}{2}} g_m[i]u_{m+i}[nT + p_s(d_{m+i} - d_m)], \quad (2)$$

where  $n$  and  $m$  are the indices for  $\tau$  and  $\eta$ , respectively;  $s$  is the index for slowness  $p$ ;  $i$  is the index for the traces within a stack which consists of traces around the target trace  $\eta$ ; and  $L$  the number of traces in that stack.  $T$  is the sampling interval, and  $d$  the distance.

As shown in eqs (1) and (2), the LSST essentially takes an input record section in the time-space domain and transforms it to the time-space slowness domain (Fig. 3). In the slowness domain,

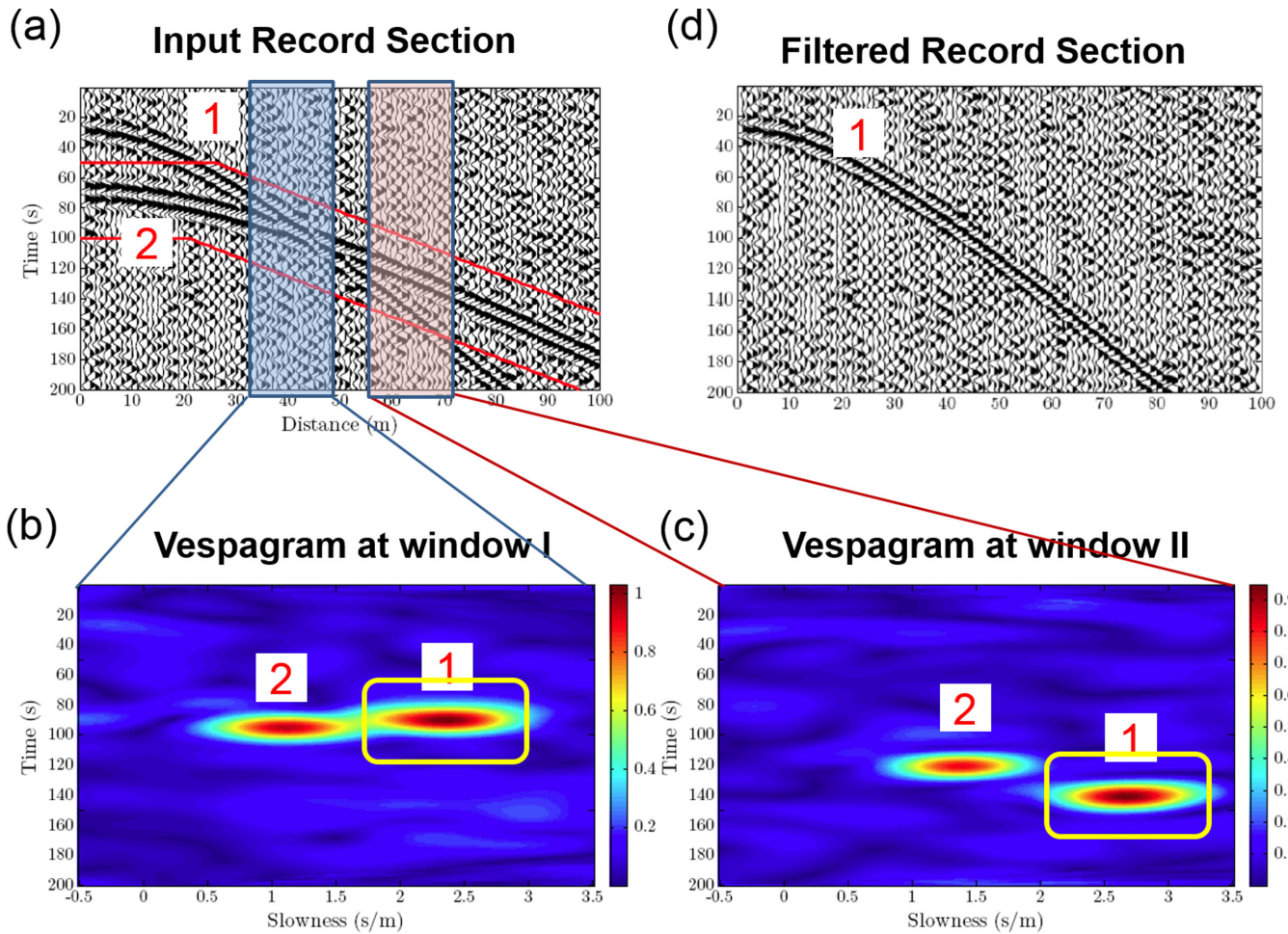


**Figure 2.** (Modified from Ventosa *et al.* 2012) An example from exploration seismology to demonstrate the basic concept of the local slant-stack filters (LSSFs). (a) Input record section containing two coherent signals marked ‘1’ and ‘2’ interfering with each other. (b) and (c) Vespagrams for two spatial windows around distances of 40 and 60 m, respectively. The difference in the slowness of the two signals ‘1’ and ‘2’ is revealed. The yellow box shows one can choose to extract signal ‘1’ and remove ‘2’ in the slowness domain. (d) After returning to the time domain, a cleaned record section is obtained with only signal ‘1’ preserved.

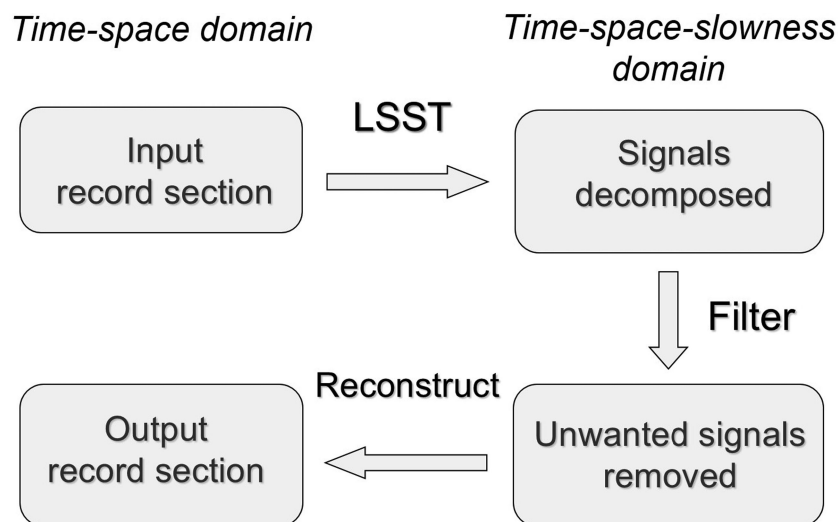


**Figure 3.** A summary of the workflow of the LSSF filtering. The left-hand column shows time–space domain, and the right column the time–space-slowness domain. In the slowness domain, one can design filters to remove signals with undesired slownesses (in other words, coherent noise), as well as random noise.

each coherent signal will form an energy peak centred at its slowness, and random noise will become low-amplitude background. One can then design specific filters, namely the LSSFs, to extract only one target slowness (or a range of slownesses) of interest and mask out the other undesired slownesses, and then transform back to the time–space domain to obtain a cleaned-up record section, in which only the signal of target slowness is preserved, whereas interfering signals with a different slowness (in other words, coherent noise) and random noise are removed (Ventosa *et al.* 2012; Ventosa & Romanowicz 2015). This is very suitable for the case of *SS* precursors, because both the expected slownesses of the *SS* precursors and those of the interfering phases are known and can be calculated for reference models such as *PREM*. Specifically, the *SS* precursors have slownesses that are very close to that of the *SS* (difference  $< \pm 0.5$  s deg $^{-1}$  predicted for *PREM*), while the interfering phases ( $S_{\text{diff}}$  postcursors and  $ScSScS$  precursors) have distinctively different slownesses (difference =  $\sim 3$ – $4$  s deg $^{-1}$ ), and can therefore be well separated from the *SS* precursors in the slowness domain.

The major advantage of the LSSF method compared to simple slant stacking comes from the property of locality and the use of coherence (instead of the stacked amplitude) in parallel to determine the optimal slowness of every phase.

Instead of stacking all traces across the entire epicentral distance range, we only stack within a small distance window in the vicinity of a given trace; such localized stacking is then repeated for all traces. Because of this locality, LSSF is able to track the local variations of the slowness of the target signal, thus providing more spatial details. In addition, unlike the simple stacking in which only one trace (and one measurement) is obtained after stacking, the LSSF produces a filtered record section from which measurements can be made on each trace, therefore significantly improves the spatial resolution (still limited by the aperture of the local stacking, as described in the following paragraph).

One key parameter of choice in designing the LSSF filters is the aperture (bin size) of local slant stacking. To achieve higher spatial resolution, a small aperture is desired. However, smaller aperture will smear the slowness resolution, making it more difficult to separate the interfering slownesses from the target slowness on the vespagram. A balance can be achieved by selecting an optimal stacking aperture in consideration of the sampling density of the array and the noise level. The details of the selection strategy is described in Ventosa *et al.* (2012) for the exploration seismology case and in Ventosa & Romanowicz (2015) for the teleseismic case. In short, the minimum aperture (bin diameter) is approximately  $A = T/\Delta p$ , where  $\Delta p$  is the slowness resolution to be achieved, and  $T$  is the dominant period of the signal. In our case, if  $\Delta p = 2.5$  s deg $^{-1}$  and  $T = 15$  s, then the bin diameter is  $A = 6^\circ$  (on the receiver side), which translates to a bin radius of  $1.5^\circ$  at the midpoint. We settle on this value for the entire data set. An even smaller radius can be attempted in certain parts of our study region where the sampling density is higher, but here we opt not to use the adaptive scheme for the sake of simplicity.

We note here that the least-squares and the high-resolution Radon transforms (An *et al.* 2007; Gu & Sacchi 2009; Schultz & Gu 2013a,b) are two possible approaches that could be used to enhance the robustness and the resolution of the slant-stack transform. Both approaches could potentially be applied on the LSST. The drawback is that they imply working in the frequency domain and setting up a set of linear inverse problems (one at each frequency) with a least squares, Chauchy or L1 norm regularization term, which is both computationally heavy, and implies the use of regulariza-

tion, which can be somewhat arbitrary. In Ventosa & Romanowicz (2015), we follow an alternative path with the slant-stacklet transform combining the slant-slack and the wavelet transforms. Despite the improvements these methods may bring, we opt for the LSST since it is simple but sufficient in the present context, and does not require operations in the frequency domain.

It is worth commenting on the linearity of the stacking scheme. There are numerous ways to enhance the detection of coherent signals. The most straightforward one is linear stacking, where the seismograms are simply summed. Alternative non-linear stacking schemes include phase weighted stacking,  $n$ th root stacking, semblance stacking, etc. Many among the latter ones tend to sharpen the peaks on the stacked trace and improve the slowness resolution, but the disadvantage is that they are often non-linear, therefore the stacked waveform is distorted, the amplitude information is not preserved (e.g. Cao & Romanowicz 2009). This can be an important concern for *SS* precursor studies, because the amplitudes of the precursors provide constraints on the impedance contrast (the product of density and seismic velocity) across the discontinuities. The density contrast is an important piece of information from the geodynamical point of view. The linearity is also required if one desires to use the precursor waveforms for forward modelling or inversion. However non-linear schemes can prove very useful due to their higher resolution and noise attenuation. We use a phase-weighted coherence estimator (non-linear) to search for the optimal slowness because this approach is not biased by the variations in the amplitude of the stacked phases (i.e. when the waveforms are equal, it gives a value up to 1 according only to their signal-to-noise ratio). In particular, we search for maxima of coherence along slowness,

$$q_m[n] = \underset{s}{\operatorname{argmax}} \frac{1}{L} \left| \sum_{i=-\frac{L-1}{2}}^{\frac{L-1}{2}} \frac{u_{m+i,s}^H[n]}{|u_{m+i,s}^H[n]|} \right|, \quad (3)$$

where  $u_{m+i,s}^H[n] = u_{m+i}^H[nT + p_s(d_{m+i} - d_m)]$  for short, and the superscript  $H$  denotes the Hilbert Transform of trace  $u$ . Linear stacking is performed in parallel in order to preserve the amplitude. We use the location of the slowness maxima, eq. (3), to select one or a few well-separated slownesses at each time for signal reconstruction. Although full inverse is more accurate, the ‘lazy’ inverse based on a single slowness component makes the inverse computationally trivial, and it is sufficient in the present context, in which the slowness of the target signal (*SS* precursors) is quasi-constant within each localized stack bin and is distinctly different from the slownesses of interfering signals and random noise. In this study, we do not present the precursor amplitude measurements, but it can be done in the future.

## 2.2 Tests on synthetic and real data

We demonstrate the effectiveness of the LSSF by applying these filters to synthetic and real data. Fig. 4 shows the results of a test of applying the filters to a synthetic record section of *SS* precursors. The locations of source and receivers are for a real 2010 May 9  $M_w$  7.2 earthquake in Sumatra and the TA station locations at the time of this earthquake, and the epicentral distances range from 120–150°. White noise with amplitudes comparable to those of the precursors is added. Specifically, the noise amplitude is 4 per cent of the *SS* main phase, whereas the  $S_{410}S$  amplitude is  $\sim 5$  per cent of the *SS*. As shown on the input record section in Fig. 4a, in the distance range 132–145°, the  $S_{410}S$  precursor suffers from interference with  $ScS_{660}ScS$ , a precursor to the  $ScSScS$ , and the

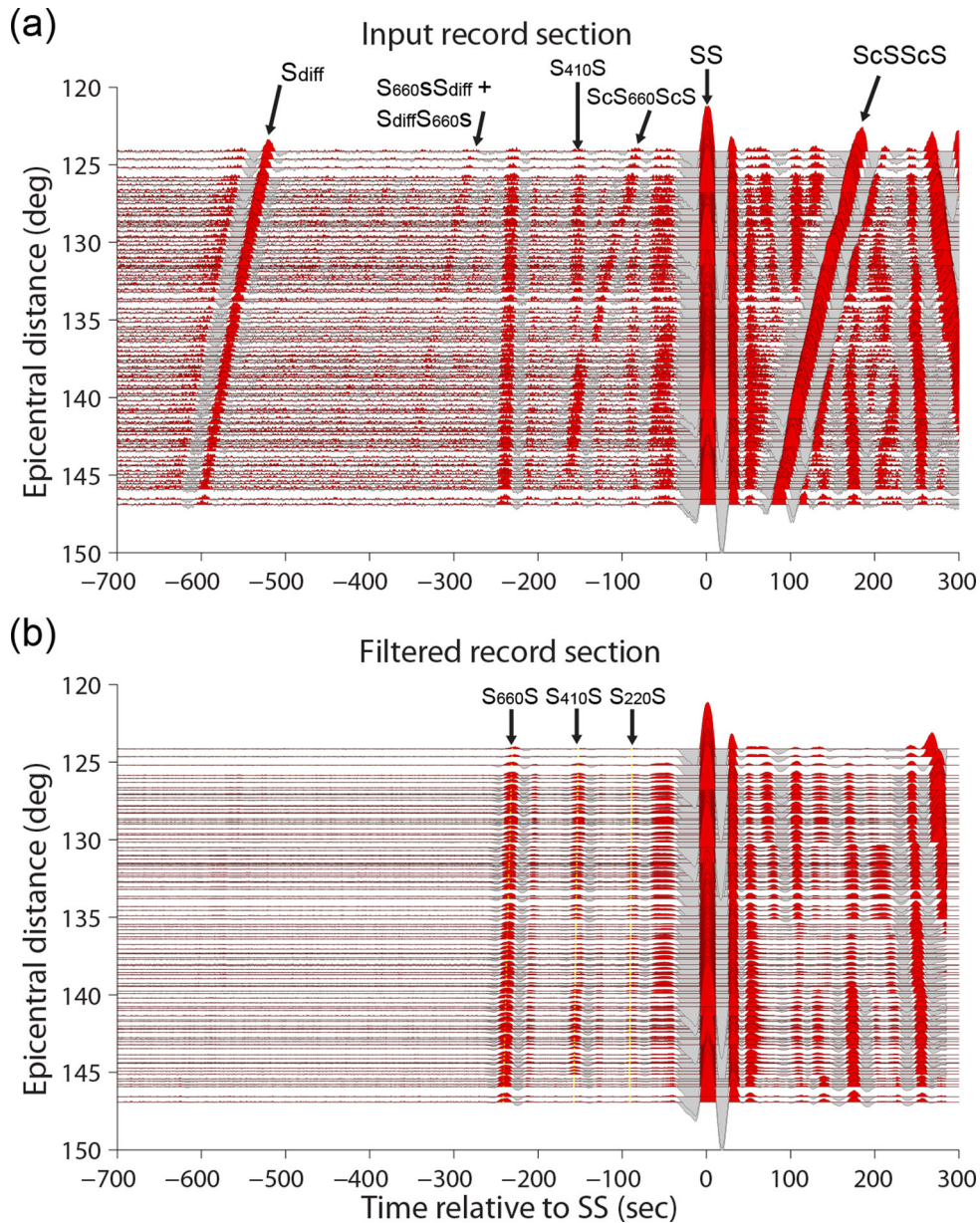


**Figure 4.** An example of the LSSF filters applied to a synthetic record section, with synthetic noise added. (a) Input record section of a 2010 May 9  $M_w$  7.2 earthquake in Sumatra. The 1-D synthetic seismograms are computed for the *PREM* model using normal mode summation; random noise with amplitude at 4 per cent of that of the *SS* main phase is then added. Relevant seismic phases are labelled. (b) Filtered record section. The seismograms are aligned on the *SS* main phase, arranged by epicentral distance. Yellow dotted lines indicate theoretical arrival times of the *SS* precursors calculated for the *PREM* model using the *TauP* toolkit (Crotwell *et al.* 1999).

interference is very severe in the distance range 138–143°, where the two signals are completely entangled. In conventional studies, data in the above-mentioned distance range for this event would have been rejected because of this interference. However, by taking advantage of the different slowness of the two phases, the LSSF filtering is able to extract the target  $S_{410}S$  phase and remove the interfering  $ScS_{660}ScS$  phase (Fig. 4b), making the entire distance range available. The waveforms of the  $S_{410}S$  precursor for a few traces in the 137–139° distance range, in which the interference is the most severe, are somewhat distorted, but the impact on precursor traveltimes measurement is minor.

Vespagrams shown in Fig. 5 give a more detailed picture of how the LSSF works in the slowness domain. For each localized bin two

types of vespagrams are generated, namely the stacked waveform amplitude and the phase-weighted coherence (definition given on the right hand side of eq. 3). The amplitude vespagram (Fig. 5a) is dominated by the large amplitude *SS* main phase, while the coherence vespagram (Fig. 5b) does not suffer from the amplitude bias. All the main phases (*SS*,  $S_{diff}$  and  $ScSScS$ ) and the related precursors (or postcursors) can be clearly identified on the coherence vespagram, and the target signals (*SS* and its precursors) are well separated from the interfering phases to be eliminated. Random noise does not form a peak on the vespagram because it does not stack constructively. LSSF then picks an optimal slowness from the coherence vespagram for each point along the time axis according to eq. (3), and filter out all the picks beyond the target range of

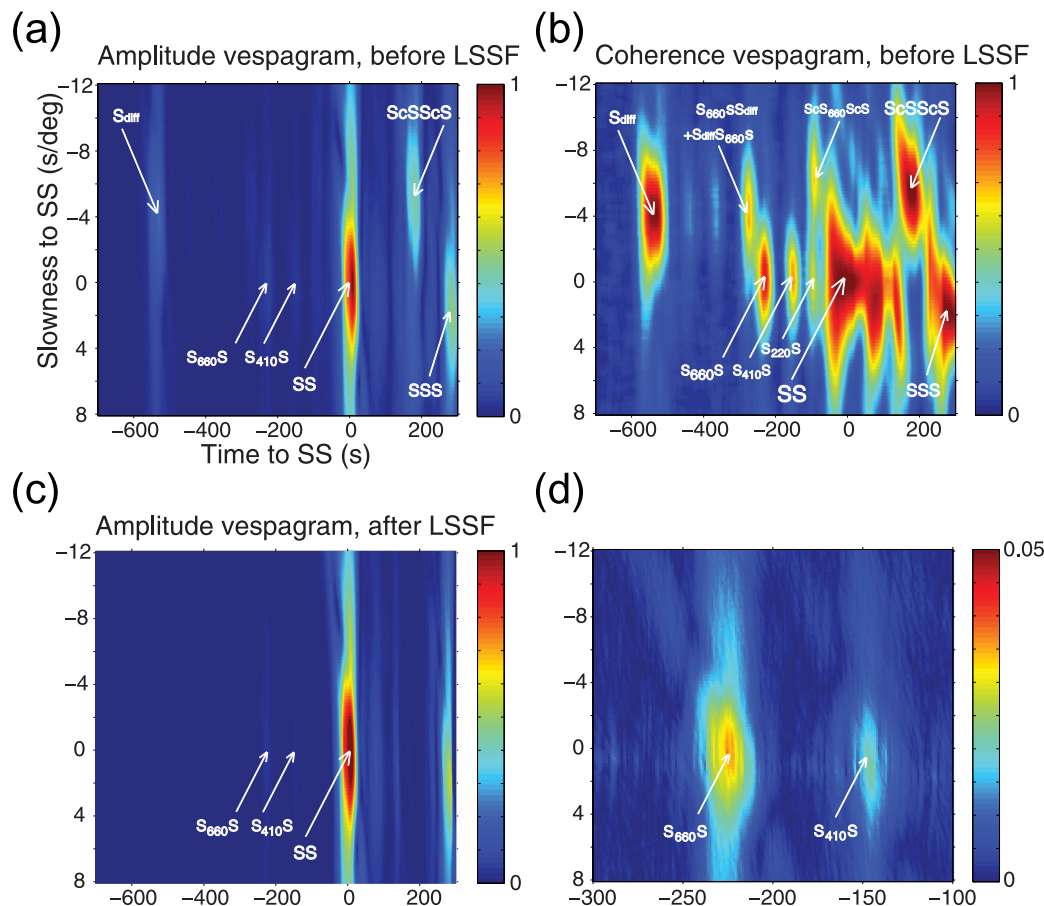


**Figure 5.** Normalized vespagrams computed by LSSF for a bin centred around a trace with  $\Delta = 125.5^\circ$  in the record section shown in Fig. 4. (a) Stacked amplitude and (b) coherence from the input record section; (c) stacked amplitude from the output record section; (d) the same as figure (c), with the time axis zoomed into the *SS* precursor time window and the colourbar adjusted to make the *SS* precursors more visible. Relevant seismic phases are labelled.

$\pm 2 \text{ s deg}^{-1}$  around the *SS* slowness. The remaining slowness picks are then used to construct the output record section (a linear process). The amplitude vespagram for the filtered record section is shown in Figs 5(c) and (d). The interfering phases are successfully removed. The amplitude of  $S_{660}S$  is stronger than  $S_{410}S$  because these are synthetic seismograms from the *PREM* model, which has a larger impedance contrast across the 660 discontinuity than the 410.

Fig. 6 shows an example of applying the LSSF to real data. Fig. 6(a) shows the record section from a 2007 December 9  $M_w$  7.8 earthquake in Fiji recorded at the TA for a specific azimuth window. The *SS* main phase is very clear. However, the *SS* precursors can hardly be identified, because they are buried in the strong coda/postcursors following the *S* waves. Given the epicentral distance range ( $80\text{--}96^\circ$ ), the *S* phase is strong, so are its post-cursors. In conventional studies, this event would have been rejected. Here we apply the LSSF filters to this record section. Only the signals within the slowness range of  $\pm 1 \text{ s deg}^{-1}$  (with respect to the slowness of *SS*) that are spatially coherent over a radius of  $1.5^\circ$  are preserved. The filtered record section is shown in Fig. 6(b). The  $S_{410}S$  and  $S_{660}S$  precursors can now be clearly identified throughout the record section. Their arrival times are in good agreement with the theoretical predictions, confirming the phase identification. To quantitatively demonstrate the improvement of the record section, in Fig. 7, we compare the traveltimes of the  $S_{660}S$  precursor measured from the record section before and after the LSSF for this event. Before the filtering (Fig. 7a), the traveltime measurements are much more scat-

tered, and the slope of the trend is in agreement with the slowness of *S*, indicating that the measurements are strongly biased by the *S* post-cursors. After filtering (Fig. 7b), the measurements are much more coherent, and have the correct traveltime and slowness. A close-up look at the measurements (Fig. 7c) shows the variation on small scales, indicating the spatial resolution power of LSSF. A few outliers are seen in Fig. 7(b), due to noise when there are too few traces in the stacking bin to generate a robust measurement. These outliers are usually associated with a low ( $<0.5$ ) cross correlation (CC) coefficient between the precursor and main *SS* waveforms, and are removed by applying a threshold of  $\text{CC} \geq 0.5$  before proceeding to further analysis. In summary, the above tests with synthetic and real data illustrate the effectiveness of the LSSF filters.

### 3 DATA AND PROCESSING

#### 3.1 The data set

Here, we systematically apply LSSF to real data recorded by the TA. We collected a data set from events in the southwestern rim of the Pacific Ocean between January 2004 and December 2013 with the following criteria:  $6.2 \leq M_w \leq 7.8$ , depth  $\leq 75 \text{ km}$ ,  $80^\circ \leq \Delta \leq 160^\circ$ . These criteria are consistent with previous *SS* precursor studies (e.g. Schmerr & Garnero 2006; Schmerr *et al.* 2010), except we relax the restriction on the epicentral distance range. One

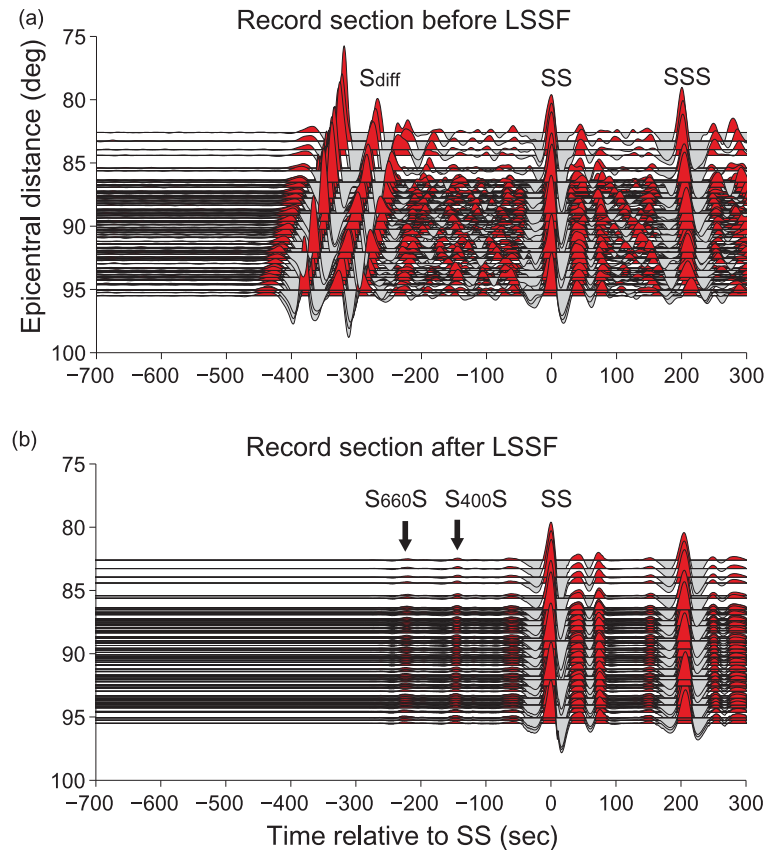


**Figure 6.** An example of applying the LSSF filters to an observed record section from a 2007 December 9  $M_w$  7.8 earthquake in Fiji. The seismograms are aligned on the *SS* main phase. (a) Input record section; (b) filtered record section.

exceptional event with a depth of 100 km is included in the data set due to excellent data quality. We look at the transverse component displacement seismograms band-pass filtered in the range 15–75 s. For data quality control, we first visually inspect the record sections to make sure the *SS* main phase is strong and clear (not nodal in radiation pattern), and the background noise level is reasonably low; then for the accepted events, we apply an automatic signal to noise ratio threshold on each trace, such that the ratio between the maximum amplitude within the *SS* precursor window and that of the *SS* main phase is less than 1/3, in order to remove the noisy traces. A total of 46 events (listed in Table 1) entered the final data set. Their *SS* precursor bounce points cover a wide region across the Pacific with high sampling density (Fig. 8). We then apply the LSSF filters event by event to clean up the record sections. In this study, we intentionally restrict ourselves to single event analysis. As a result, the larger magnitude earthquakes are generally favoured due to better signal-to-noise ratio. We do not stack across multiple events in order to avoid the complexity that comes from the variability of source duration, source time function shape, focal depth, etc. across different events, which can greatly distort the stacked waveforms and lead to biased traveltime measurements. This is more of a concern because we use larger magnitude events. One way to address the source complexity is to deconvolve the *SS* main phase from the precursor waveforms before stacking (e.g. Gurrrola & Rogers 2013; Schultz & Gu 2013a,b).

The aperture of local slant stacking is determined based on the balance between desired spatial resolution and the quality of data. In this study, given the typical hit count density, the signal to noise

ratio, and the frequency content of the *SS* precursor signals, we choose an optimal aperture (bin radius) of  $1.5^\circ$ . This value is fixed for all events.

### 3.2 From traveltime to discontinuity depth

Differential traveltimes between the *SS* main phase and a precursor (410 or 660) are then measured using cross correlation from each trace in the LSSF filtered record sections. A time window of  $[-20, 20]$  second around the *PREM* predicted arrival time is used for the cross correlation for each target phase, with the exception that a window of  $[-10, 30]$  second is used for the 660 precursor, in order to account for the fact that *PREM* assigns a slightly deeper nominal depth of 670 km to the 660-discontinuity.

We calculate corrections for these traveltimes due to: (1) bathymetry/topography of the free surface, (2) variations in Moho depth and (3) 3-D heterogeneities in the mantle. For bathymetry/topography, we use *ETOPO5* (Edwards 1989) smoothed on a  $1 \times 1^\circ$  global grid. For Moho depth, we use *CRUST1.0* (Laske *et al.* 2013), which is also gridded  $1 \times 1^\circ$ . For 3-D mantle corrections, we use a very recent whole mantle tomographic model *SEM-UCBwm1* (French & Romanowicz 2014). These traveltime corrections are calculated cumulatively along each ray path in the 1-D Earth model. For ray tracing, the *TauP* toolkit (Crotwell *et al.* 1999) is used, and the model is *PREM* (Dziewonski & Anderson 1981). The results of these corrections are summarized in Fig. 9. The free surface and crustal corrections are on the order of a

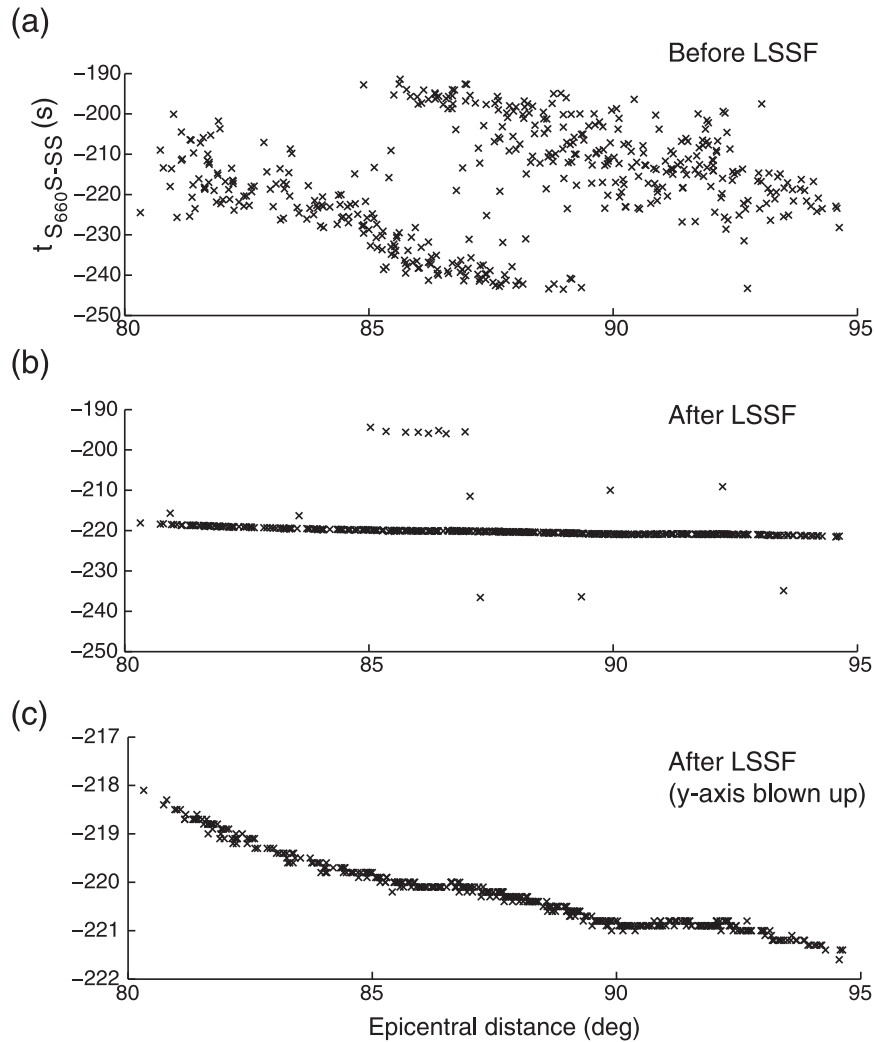


**Figure 7.** Differential traveltimes of  $S_{660}S-SS$  measured from (a) the input and (b) the filtered record sections shown in Fig. 6. The traveltimes are measured by cross-correlation between the  $S_{660}S$  and  $SS$  waveforms. Panel (c) is the same as (b) except for a much smaller  $y$ -axis range to show the undulation of measurements on smaller scales.

few seconds mainly within the oceanic regions, and the mantle corrections are on the order of 2–3 s. These trends are consistent with previous global  $SS$  precursor studies (e.g. Bai *et al.* 2012) as well as a regional scale study for the central Pacific (Schmerr & Garnero 2007). One point to keep in mind is that here we use 1-D ray tracing, which assumes that the ray paths of  $SS$  and its precursors are not perturbed by 3-D heterogeneity, which is only true to first order. In reality, large scale heterogeneities can alter the ray paths (Zheng & Romanowicz 2012) and may result in larger traveltime perturbations in certain cases.

After the above corrections have been made, the precursor traveltime measurements are then converted to discontinuity depths at the bounce point for each ray path. A 1-D velocity model is needed for the time to depth conversion; here we use *PREM* (Dziewonski & Anderson 1981). Choosing a different 1-D model could change the absolute depths of the discontinuities by a few kilometres, but has little impact on the topography (lateral change in the relative depths of the discontinuities). After the measurements from each point have been obtained, they are then combined to form a map of discontinuity topography for the entire study region.

#### 4 RESULTS AND DISCUSSION

In this section, maps of 410 and 660 discontinuity depths as well as the mantle transition zone thickness are presented. We remind the readers that in the simplest case where the discontinuity depth change is purely caused by a thermal anomaly, a cold anomaly (e.g. subducted slab) will result in an uplifted 410 and a depressed 660, while a warm anomaly (e.g. upwelling) will cause a deepened 410 and a shallower 660. The colour convention of our discontinuity topography maps (Figs 10 and 11) will reflect this thermal-origin assumption. We also note that there may exist other complication factors besides the simple thermal interpretation, such as compositional anomaly, and/or the effect of remaining 3-D volumetric heterogeneities that are not fully accounted for by the traveltime corrections described in the previous section. We then compare the 410 and 660 topography maps to two recent global 3-D mantle shear wave velocity models, the upper mantle model *SEMum2* (French *et al.* 2013) and the whole mantle model *SEM-UCBwm1* (French & Romanowicz 2014), to discuss possible fine-scale correlations. These high resolution tomography models were developed from full-waveform inversion based on the Spectral Element method

**Table 1.** A list of the 46 earthquakes used in this study.

Evt#	Date	Time	Longitude	Latitude	Dep (km)	$M_w$
1	2005/01/01	06:25:44	5.1	92.3	12	6.7
2	2005/04/11	12:20:06	-3.48	145.91	11	6.7
3	2006/03/14	06:57:33	-3.6	127.21	30	6.7
4	2007/01/30	04:54:50	-54.74	146.3	11	6.9
5	2007/02/20	08:04:25	-1.03	126.98	11	6.8
6	2007/06/28	02:52:09	-7.97	154.63	10	6.7
7	2007/09/30	05:23:34	-49.27	164.12	10	7.4
8	2007/11/10	01:13:29	-51.78	161.32	10	6.6
9	2008/02/13	19:58:46	-8.16	128.64	19	6.2
10	2008/03/20	14:10:44	6.18	126.93	82	6.1
11	2008/06/01	14:31:03	-59.38	149.66	10	6.5
12	2008/08/30	06:54:07	-6.15	147.26	75	6.4
13	2008/10/23	10:04:35	-2.63	145.57	10	6.4
14	2009/02/11	17:34:50	3.88	126.4	22	7.2
15	2009/02/12	03:49:39	3.95	126.41	26	6.1
16	2009/02/12	13:15:06	4.04	126.55	26	6.3
17	2009/03/16	14:15:56	3.81	126.55	35	6.4
18	2009/08/10	19:55:35	14.1	92.89	5	7.5
19	2009/09/18	06:23:53	12.62	120.43	12	6.0
20	2009/10/01	01:52:27	-2.52	101.5	10	6.6
21	2009/11/08	19:41:43	-8.21	118.63	18	6.7
22	2010/03/14	00:57:44	-1.69	128.13	53	6.5
23	2010/06/12	19:26:50	7.88	91.94	35	7.5
24	2010/07/21	09:16:04	3.04	128.22	100	6.1
25	2010/09/29	17:11:25	-4.96	133.76	26	7.0
26	2011/04/23	04:16:55	-10.35	161.23	82	6.9
27	2011/10/14	03:35:14	-6.57	147.88	37	6.5
28	2012/07/25	00:27:45	2.71	96.04	22	6.4
29	2012/07/25	11:20:27	-9.69	159.73	20	6.5
30	2012/07/28	20:03:56	-4.65	153.17	41	6.6
31	2012/08/31	12:47:33	10.81	126.64	28	7.7
32	2012/09/08	10:51:44	-3.18	135.11	21	6.2
33	2012/09/14	04:51:47	-3.32	100.59	19	6.3
34	2012/10/09	12:32:09	-60.33	153.7	10	6.6
35	2012/12/17	09:16:30	-0.65	123.81	44	6.1
36	2013/02/08	11:12:11	-10.84	165.97	12	6.9
37	2013/03/10	22:51:50	-6.6	148.17	28	6.6
38	2013/04/06	04:42:35	-3.52	138.48	66	7.0
39	2013/04/23	23:14:42	-3.91	152.13	16	6.5
40	2013/07/21	05:09:31	-41.7	174.34	17	6.5
41	2013/08/06	10:41:30	-22.5	173.8	10	5.9
42	2013/08/16	02:31:05	-41.73	174.15	8	6.6
43	2013/09/30	05:55:55	-30.88	-178.38	42	6.4
44	2013/10/15	00:12:32	9.88	124.12	19	7.1
45	2013/11/19	13:32:54	2.65	128.4	64	6.1
46	2013/12/01	01:24:14	-7.01	128.35	10	6.5

(Capdeville *et al.* 2003), and the spatial resolution at the transition zone depths is on the order of  $\sim 600$  km horizontally.

#### 4.1 The 410 discontinuity topography

Fig. 10(a) shows a map of the 410 discontinuity depth in the study region. Warm colours represent a longer  $SS-S_{410}S$  differential travel-time, or equivalently, an apparently deeper 410, suggesting a warm anomaly if explained only by a temperature effect on the olivine phase transformation. Cold colours, on the contrary, indicate a shorter  $SS-S_{410}S$  time, or an apparently shallower 410, suggesting a presumably cold anomaly.

Overall the 410 discontinuity is relatively flat throughout the region except for a few hotspots in the central and southern Pacific

and the subduction margin at the Pacific Northwest. This is consistent with previous global studies (e.g. Flanagan & Shearer 1998; Gu *et al.* 2003; Chambers *et al.* 2005; Lawrence & Shearer 2008) as well as a regional study specifically for the Pacific ocean (Schmerr *et al.* 2010). The very long wavelength structure is characterized as a three-stage variation from small or fair deepening in northeastern Eurasia, to uplift in the northwestern Pacific Ocean, to significant deepening in the hotspot regions in the central and south Pacific. This trend agrees very well with the global 410 topography imaged by Chambers *et al.* (2005), where both  $PP$  precursors and  $SS$  precursors were used and the two data sets produced consistent long wavelength images. The average 410 discontinuity depth for our study region is 406 km, with a standard deviation of 10 km. It is somewhat shallower than the average of 416 km reported by Schmerr *et al.* (2010), but the difference could simply come from

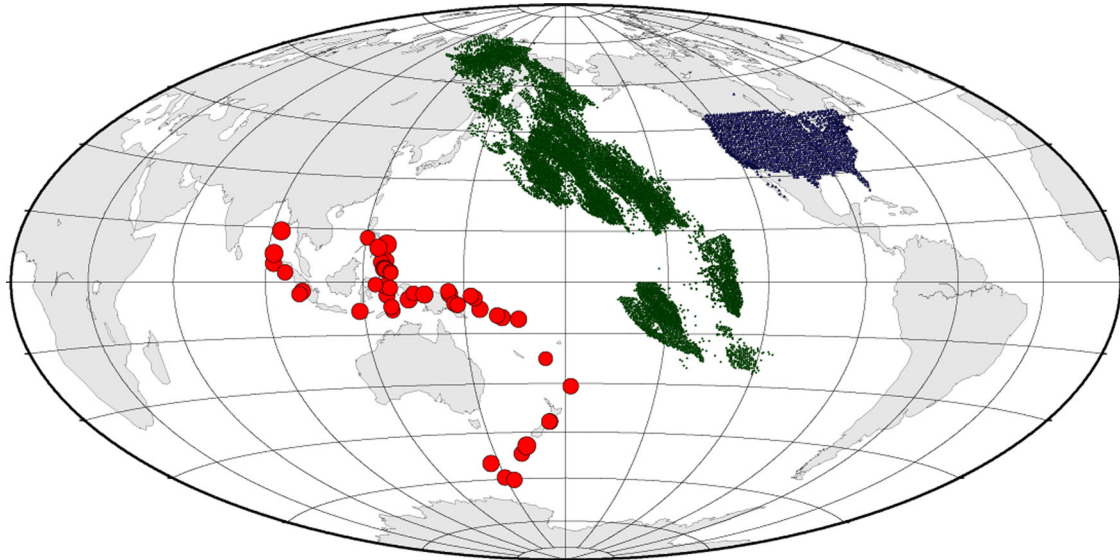


**Figure 8.** A map showing the data set of 46 earthquakes (detailed information listed in Table 1) with high-quality *SS* precursor record sections recorded by the U.S. Transportable Array. The source locations are shown by red circles, the stations by blue triangles, and the *SS* bounce points by dark green dots.

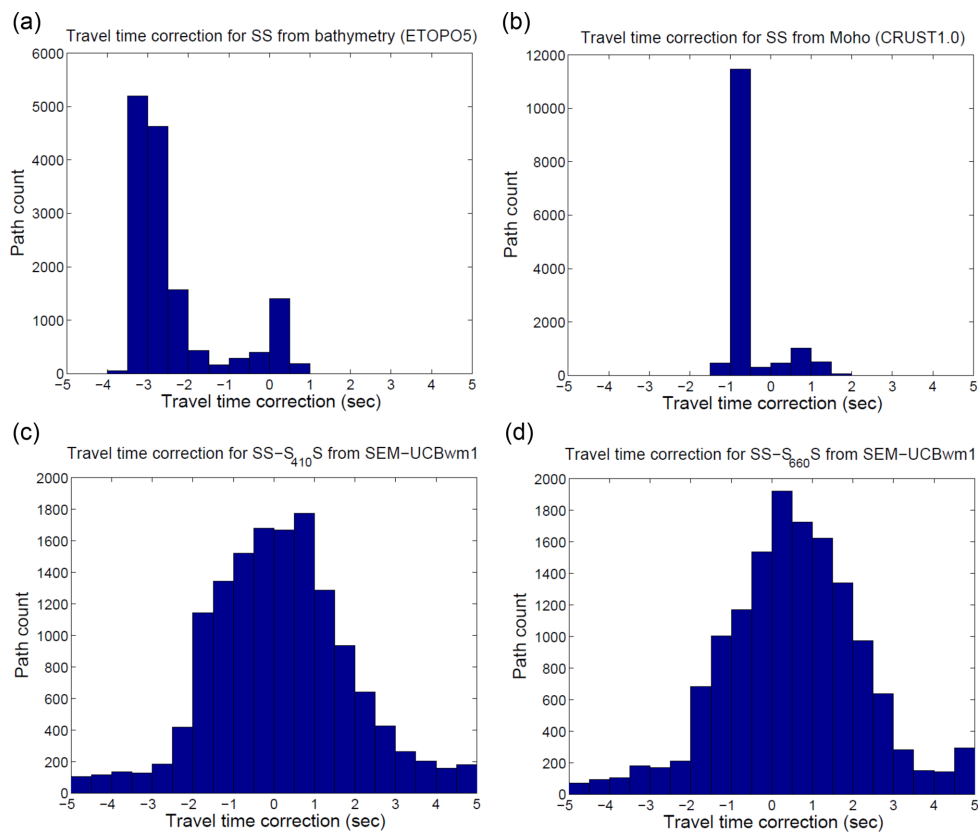


**Figure 9.** Corrections to *SS* and the precursor traveltimes due to (a) surface topography/bathymetry, (b) variation in Moho depth, (c) and (d) 3-D velocity structure in the mantle. For topography/bathymetry, *ETOPO5* (Edwards 1989) model is used. For Moho depth, *CRUST1.0* (Laske *et al.* 2013) model is used. For 3-D mantle structure, the whole-mantle shear wave model *SEM-UCBwm1* (French & Romanowicz 2014) is used.

the fact that the latter is taken from the entire Pacific Ocean, while this study only covers a swath of it. With uncertainty included, our result is in rough agreement with the global average of  $\sim 410$  km (e.g. Chambers *et al.* 2005).

A few small scale warm anomalies are seen on the map (circled out and labelled ‘A’ through ‘D’ on Fig. 10a), with variable size and strength. Interestingly, the locations of these anomalies coincide

with a few low velocity columns penetrating the 410 discontinuity as revealed by the upper mantle tomography model, *SEMum2* (French *et al.* 2013), shown in Figs 10(b) and (c). These low velocity columns in *SEMum2* are explained as hot material rising from the lower mantle, which would have a ‘warm’ signature on the 410 topography. It is remarkable that not only the geographical locations, but also the horizontal extent and the strength of the anomalies are

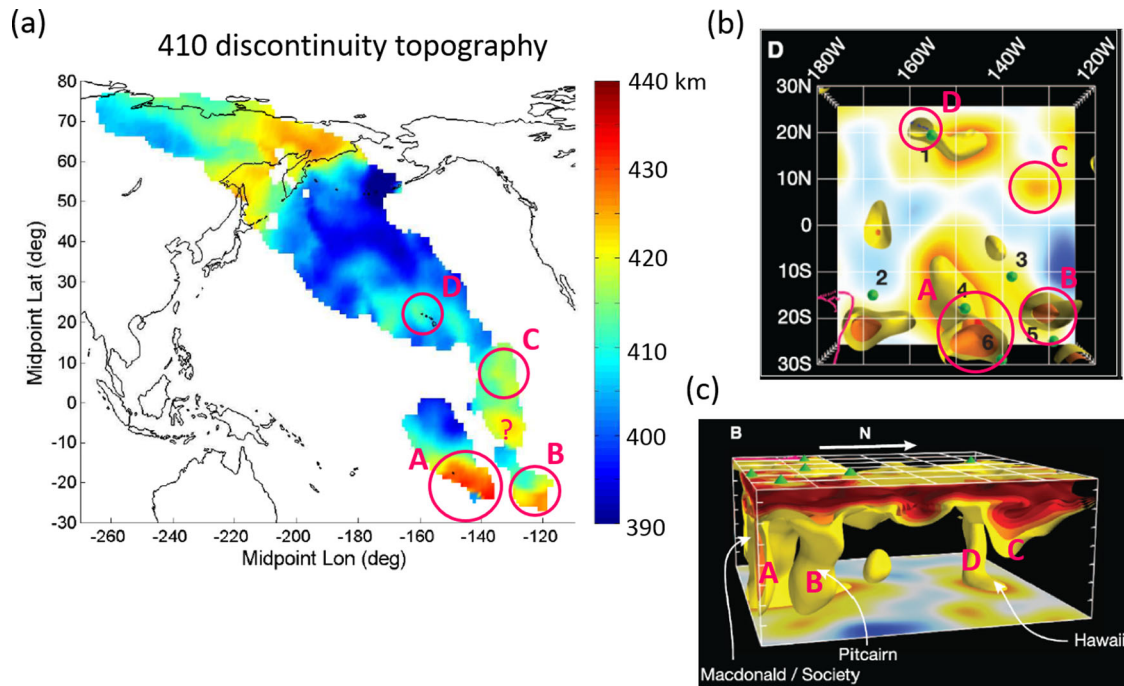


**Figure 10.** (a) A map of the 410 discontinuity topography converted from precursor traveltimes after crust and mantle correction. Warm colours represent longer  $SS-S_{410S}$  differential traveltimes, or equivalently, an apparently deeper 410, suggesting a warm anomaly if explained by temperature effect alone on the olivine phase transformation. Cold colours, on the contrary, indicate a shorter  $SS-S_{410S}$  time, or an apparently shallower 410, suggesting a cold anomaly. Panels (b) and (c) Shear wave tomographic images for part of the study region shown in (a). The images are modified from French *et al.* (2013), for the upper mantle model *SEMum2*. Low shear velocity ( $>2$  per cent  $V_s$  reduction) bodies are shown in yellow contours. The circled areas labelled A, B, C and D show geographic locations at which both a ‘warm’ anomaly in the 410 topography and a slow velocity anomaly in the tomography model are observed.

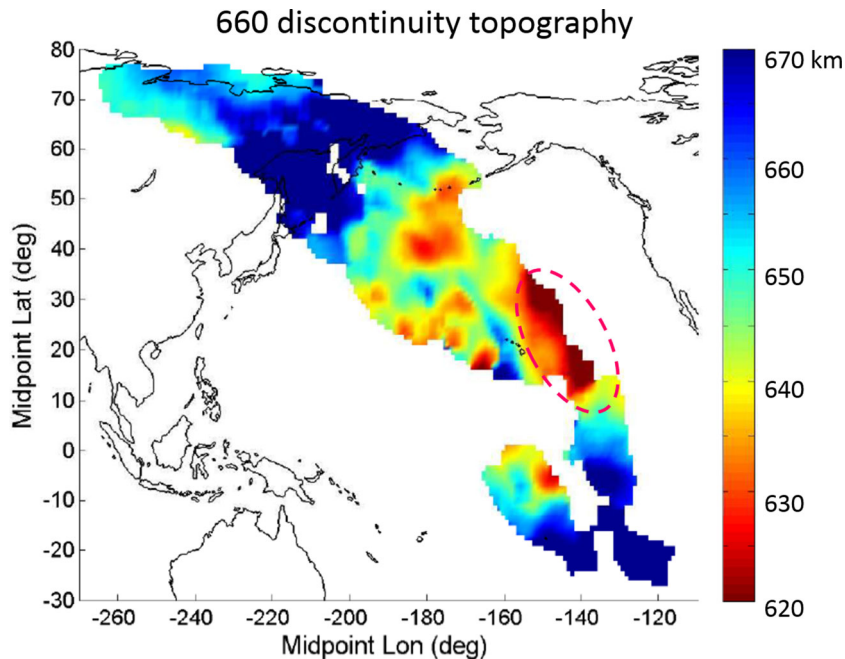


**Figure 11.** A map of the 660 discontinuity topography after crust and mantle traveltime correction. The dashed oval outlines an anomalous area to the east of Hawaii, for which significantly shorter  $SS-S_{660S}$  differential traveltimes are observed. Note the sense of colourbar is opposite to Fig. 10 to reflect the simple assumption of thermal effect.

in good agreement between the 410 topography and the tomography images, which have been developed using totally independent data. The remarkable correlation between the two gives us confidence to interpret the fine-scale features from both images. Note that the 3-D mantle correction using *SEM-UCBwm1* (very close to *SEMum2*

in the upper mantle) does not eliminate the correlation between the 410 topography and the tomography at the hotspots, suggesting these anomalous 410 depressions has an origin apart from mantle heterogeneity, likely a temperature increase associated with the upwelling.

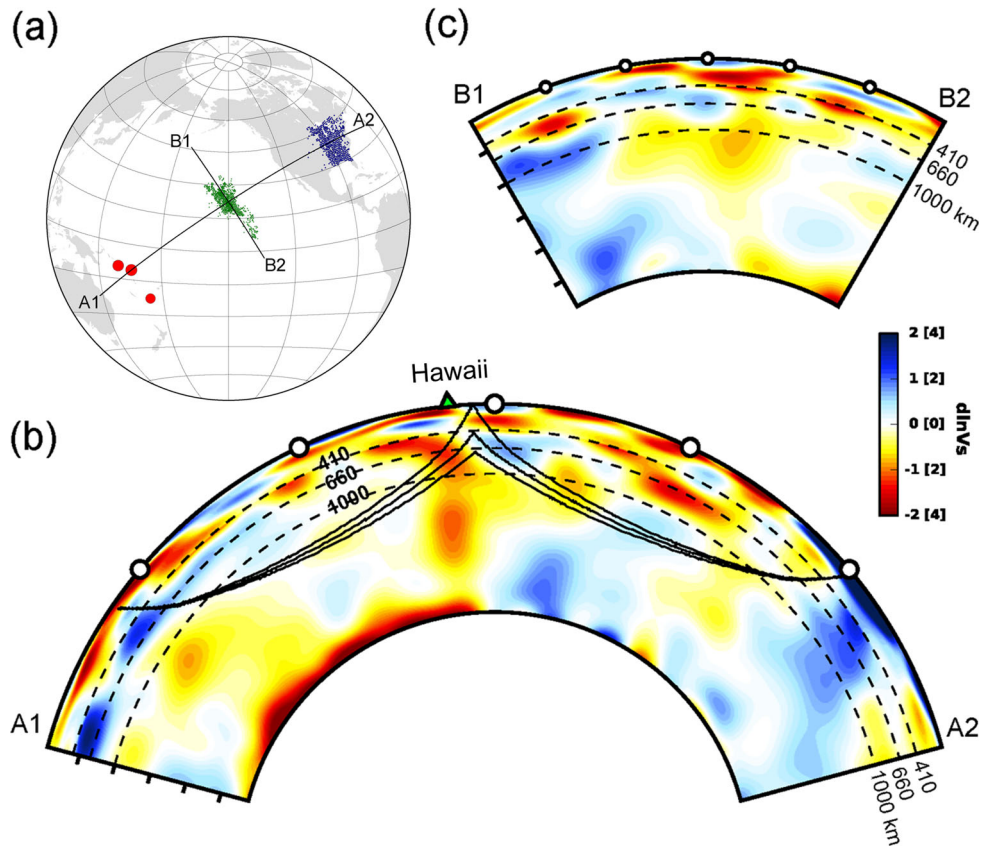


**Figure 12.** (a) A map showing the three events that sample the anomalous area outlined in Fig. 10. The event locations are shown by red circles, the stations by blue triangles, and the SS bounce points by green dots. (b) Cross section along the great circle plane A1–A2, from the whole mantle shear wave tomography model *SEM-UCBwm1* (French & Romanowicz 2014). The ray paths of the SS and its precursors for a representative receiver are shown. (c) Cross section along Profile B1–B2, which is perpendicular to Profile A1–A2.

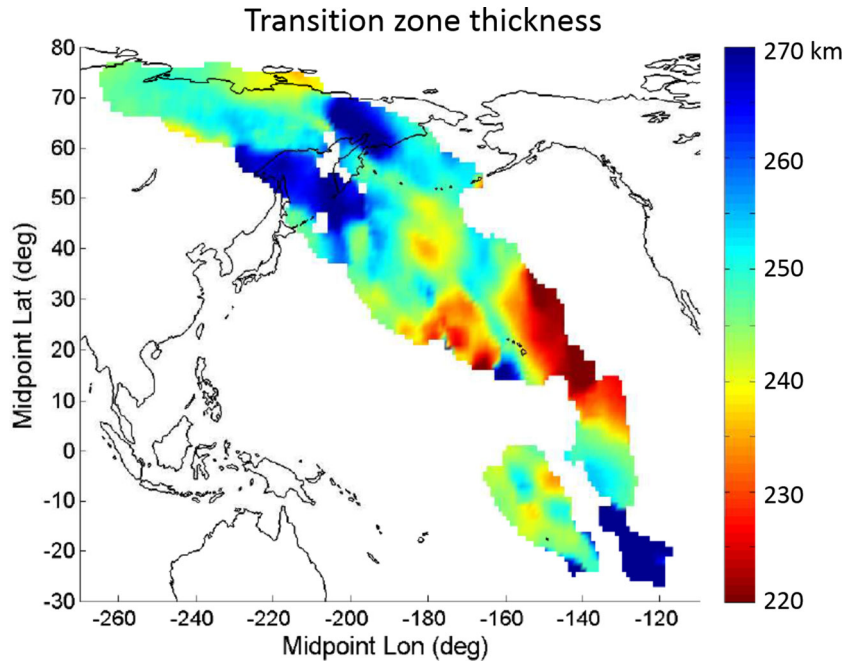
#### 4.2 The 660 discontinuity

Fig. 11 shows a map of the 660 discontinuity depth. Warm colours represent a shortened (opposite to the convention used for 410)  $SS-S_{660}S$  differential traveltime, or equivalently an apparently shallower 660 consistent with a warm temperature anomaly. Cold colours, on the other hand, suggest a cold anomaly.

Overall the 660 discontinuity shows larger topography than the 410. The depth of the 660 is significantly depressed beneath the colder subduction zones at the northwestern rim of the Pacific Ocean, and uplifted within the warmer oceanic regions. These are again in good agreement with other previous studies (e.g. Flanagan & Shearer 1998; Gu *et al.* 2003; Lawrence & Shearer 2008; Houser & Williams 2010; Schmerr *et al.* 2010). Our average depth is at  $648 \pm 20$  km, which is in good agreement with the global average of  $\sim 650$  km and the Pacific average of 658 km reported by Schmerr *et al.* (2010). The deepest discontinuity is seen beneath the northwestern Pacific subduction, where it is inferred that the ponded slab has caused a widespread depression of the 660 discontinuity also observed by several previous regional studies (Heit *et al.* 2010; Schmerr & Thomas 2011; Gu *et al.* 2012). The maximum depth reaches  $\sim 680$  km, in very good agreement with a regional study by Gu *et al.* (2012). In the central and south Pacific, the 660 discontinuity is generally uplifted, again consistent with previous regional studies (Schmerr & Garnero 2006; Schmerr *et al.* 2010). One striking feature on the 660 topography map is an area of extremely ‘warm’ anomaly (depth at  $\sim 620$  km) to the east of Hawaii, outlined

by a dashed oval in Fig. 11. Past global studies have documented a similar anomaly to the east or southeast of Hawaii, although the magnitude of the depression is milder (depth at  $\sim 640$  km), which could be explained by damping due to larger stacking bin size because of sparser data. A recent study by Yu *et al.* (2013) using the Transportable Array data has observed this anomaly, with a magnitude (depth at  $\sim 620$  km) very close to our result. The authors applied both common-midpoint stacking and the more sophisticated Generalized Radon Transform, and both methods produce essentially identical results. In our data set, this anomalous area is sampled by three events from somewhat different azimuths (Fig. 12a), and all three events give consistent results, suggesting it is a robust observation. Given the magnitude of this topography, if explained by thermal effects alone, it would require a temperature anomaly too large to be physically probable. Other possible causes of this apparent topography include large scale heterogeneities in the mantle. Gu *et al.* (2003) and Zhao & Chevrot (2003) discussed the trade-off between volumetric velocity anomaly and discontinuity topography in terms of their effect on SS precursor traveltimes from a theoretical point of view. Zheng & Romanowicz (2012) showed a case of observation in which large scale heterogeneities (the Rocky Mountain Front specifically) has a significant impact on the precursor waveforms. Here, to explore possible impact from mantle heterogeneities, we look at cross sections of the whole mantle tomography model *SEM-UCBwm1* (French & Romanowicz 2014).

Two sections are shown in Fig. 12, one along the great circle plane (Fig. 12b) containing the SS and precursor ray paths for one



**Figure 13.** A map of the mantle transition zone thickness in the study region, after crust and mantle traveltime correction.

of the three events that sample the above-mentioned 660 anomaly, the other one perpendicular to the plane (Fig. 12c) at the SS bounce point. One prominent feature shown by the in-plane section A1–A2 is a large east-dipping low velocity body in the transition zone and the underlying uppermost lower mantle beneath Hawaii. This low velocity body stretches eastward for a distance of  $\sim 1500$  km while dipping to a depth of  $\sim 1000$  km. Below 1000 km, it is connected to a nearly vertical plume originated from the lower mantle, with a faint low velocity tail dipping eastward for a fairly long horizontal distance. Above and east of this low velocity tail is a fast anomaly. At much shallower depths (200–400 km), another low velocity anomaly is present, which has also been observed in regional studies (e.g. Wolfe *et al.* 2009). To explore the relationship between the SS precursors and these mantle heterogeneities, in Fig. 12(b), the theoretical ray paths of SS,  $S_{410}S$  and  $S_{660}S$  for a representative receiver (approximately at the centroid of all the receivers) are overlain on the tomographic image. The  $S_{660}S$  precursor grazes the upper boundary of the east-dipping low velocity body and the eastward-dipping tail for a fairly long distance, whereas the  $S_{400}S$  and the SS traverses through the fast anomaly above. This would predict a significantly delayed  $S_{660}S$  absolute traveltime and advanced  $S_{410}S$  and SS traveltimes. In terms of differential traveltime, this would result in a significantly longer SS– $S_{660}S$  time and a more or less normal SS– $S_{410}S$  time. When converted from time to depth, this would predict an apparently normal 410 depth and a significantly shallower (or apparently ‘warmer’) 660, which agrees very well with what is observed on our discontinuity maps in Figs 10 and 11.

### 4.3 The mantle transition zone thickness

Compared to the individual discontinuity depths, the transition zone (TZ) thickness is a supposedly more robust measurement. By taking the traveltime difference between the 410 and 660 precursors, the impacts of the surface topography and/or bathymetry, the crust and the uppermost mantle structure on the two precursors are largely

cancelled out. For this reason, most discontinuity topography studies choose to present their results in the form of TZ thickness.

A map of the TZ thickness for our study region is shown in Fig. 13. At the long wavelengths, it is characterized by the transition from small to fair thickening beneath Siberia, to significant deepening in the subduction margin, to small or no thickening in the northwestern Pacific Ocean, to significant thinning around Hawaii, to less or no thinning further south of Hawaii. This overall trend is very consistent with previous global studies (e.g. Flanagan & Shearer 1998; Gu *et al.* 2003; Lawrence & Shearer 2008). Within the Pacific ocean, the 660 topography play a larger role than the 410 in determining the TZ thickness, which is also consistent with previous studies (e.g. Lawrence & Shearer 2008; Schmerr *et al.* 2010). The average TZ thickness for the study region is found to be  $\sim 242$  km, which is in very good agreement with the global average within 240–245 km (Flanagan & Shearer 1998; Gu *et al.* 1998; Deuss & Woodhouse 2002; Gu & Dziewonski 2002; Houser *et al.* 2008; Lawrence & Shearer 2008) and the Pacific average at 242 km (Schmerr *et al.* 2010). The standard deviation is 15 km, larger than the 5–10 km reported by previous studies. It results from the combination of a larger peak-to-peak variation (the widespread thinning to the east of the Pacific and the thickened subduction margin) and a smaller sampling area. On the finer scales, a feature worth noting is a small area of thinned TZ in the northwestern Pacific Ocean located approximately halfway between Hawaii and Kamchatka. The same anomaly has been clearly imaged by several previous studies (e.g. Gu *et al.* 2003; Houser *et al.* 2008; Lawrence & Shearer 2008), although the magnitude varies from study to study. The data coverage is dense for this area, so it should be a robust observation. However, the cause of this anomaly remains unclear.

## 5 CONCLUSIONS

We present high resolution topography images of the 410 and 660 discontinuities for a vast region across the Pacific Ocean obtained from the measurement of SS precursor traveltimes. The high density

U.S. Transportable Array data in combination with a new processing technique, namely the LSSFs, have allowed for higher spatial resolution than previous studies using simple common midpoint stacking method. Reasonable correlations are observed between several fine-scale features in our discontinuity images and corresponding velocity anomalies in the recent high resolution global mantle tomography models *SEMum2* and *SEM-UCBwm1*.

The LSSF is a powerful tool for cleaning up the otherwise very noisy *SS* precursor record sections. It enables us to extract the weak yet coherent precursor signals while removing interfering seismic phases as well as random noise, yielding reliable precursor travel-time measurements from single traces within an array, which significantly improves the spatial resolution. We recognize that the cleaned record sections can also be used as input data for other array imaging techniques such as migration (e.g. Thomas & Billen 2009; Schmerr & Thomas 2011), or for a joint inversion along with tomographic data to simultaneously constrain volumetric velocity anomaly and discontinuity topography (e.g. Gu *et al.* 2003; Houser *et al.* 2008).

It is worth pointing out that the LSSF filtering is a linear process by construction, so the amplitudes of the precursors are preserved, which is essential for reliable estimate of the impedance (and density) contrast across the discontinuities. Amplitude measurements could be carried out in a future follow-up study.

## ACKNOWLEDGEMENTS

We would like to thank Editor Christine Thomas, reviewers Nicholas Schmerr and Jeffrey Gu for providing very helpful comments on the manuscript. We thank Scott French for providing the tomography model *SEM-UCBwm1*. Waveform data used in this study were downloaded from the IRIS data centre. This work was supported by NSF EAR grant # 0738284 and ERC Advanced Grant ‘WAVE-TOMO’. This is BSL contribution 2015-02.

## REFERENCES

- An, Y., Gu, Y.J. & Sacchi, M., 2007. Imaging mantle discontinuities using least-squares Radon transform, *J. Geophys. Res.*, **112**, B10303, doi:10.1029/2007JB005009.
- Bai, L., Zhang, Y. & Ritsema, J., 2012. An analysis of *SS* precursors using spectral-element method seismograms, *Geophys. J. Int.*, **188**, 293–300.
- Bina, C. & Helffrich, G., 1994. Phase transition Clapeyron slopes and transition zone seismic discontinuity topography, *J. geophys. Res.*, **99**, 15 853–15 860.
- Bohlen, T., Kugler, S., Klein, G. & Theilen, F., 2004. 1.5D inversion of lateral variation of Scholte-wave dispersion, *Geophysics*, **69**, 330–344.
- Cao, A. & Romanowicz, B., 2009. Constraints on shear wave attenuation in the Earth’s inner core from an observation of PKJKP, *Geophys. Res. Lett.*, **36**, L09301, doi:10.1029/2009GL038342.
- Cao, Q., van der Hilst, R.D., de Hoop, M.V. & Shim, S.-H., 2011. Seismic Imaging of Transition Zone Discontinuities Suggests Hot Mantle West of Hawaii, *Science*, **332**, 1068–1071.
- Cao, Q., Wang, P., van der Hilst, R.D., de Hoop, M.V. & Shim, S.-H., 2010. Imaging the upper mantle transition zone with a generalized Radon transform of *SS* precursors, *Phys. Earth planet. Inter.*, **180**(1–2), 80–91.
- Capdeville, Y., To, A. & Romanowicz, B., 2003. Coupling spectral elements and modes in a spherical Earth: an extension to the ‘sandwich’ case, *Geophys. J. Int.*, **154**(1), 44–57.
- Chambers, K., Woodhouse, J.H. & Deuss, A., 2005. Topography of the 410-km discontinuity from *PP* and *SS* precursors, *Earth planet. Sci. Lett.*, **235**(3), 610–622.
- Contenti, S., Gu, Y.J., Ökeler, A. & Sacchi, M.D., 2012. Shear wave reflectivity imaging of the Nazca-South America subduction zone: stagnant

- slab in the mantle transition zone?, *Geophys. Res. Lett.*, **39**, L02310, doi:10.1029/2011GL050064.
- Crotwell, H.P., Owens, T.J. & Ritsema, J., 1999. The *TauP* Toolkit: flexible seismic travel-time and ray-path utilities, *Seism. Res. Lett.*, **70**, 154–160.
- Debayle, E. & Ricard, Y., 2012. A global shear velocity model of the upper mantle from fundamental and higher Rayleigh mode measurements, *J. geophys. Res.*, **117**, B10308, doi:10.1029/2012JB009288.
- Deuss, A., 2009. Global observations of mantle discontinuities using *SS* and *PP* precursors, *Surv. Geophys.*, **30**, 301–326.
- Deuss, A. & Woodhouse, J.H., 2002. A systematic search for upper mantle discontinuities using *SS*-precursors, *Geophys. Res. Lett.*, **29**, 901–904.
- Dziewonski, A.M. & Anderson, D.L., 1981. Preliminary reference Earth model, *Phys. Earth planet. Inter.*, **25**, 297–356.
- Edwards, M.O., 1989. Global Gridded Elevation and Bathymetry (ETOPO5) Digital Raster Data on a 5-Minute Geographic (lat × lon) 2160 × 4320 (centroid-registered) Grid, National Oceanic and Atmospheric Administration.
- Flanagan, M.P. & Shearer, P., 1998. Global mapping of topography on transition zone velocity discontinuities by stacking of *SS* precursors, *J. geophys. Res.*, **103**(B2), 2673–2692.
- French, S. & Romanowicz, B., 2014. Whole-mantle radially anisotropic shear velocity structure from spectral-element waveform tomography, *Geophys. J. Int.*, **199**, 1303–1327.
- French, S., Lekic, V. & Romanowicz, B., 2013. Waveform tomography reveals channelled flow at the base of the oceanic asthenosphere, *Science*, **342**(6155), 227–230.
- Fukao, Y., Obayashi, M., Nakakuki, T. & Deep Slab Project Group, 2009. Stagnant slab: a review, *Annu. Rev. Earth planet. Sci.*, **37**, 19–46.
- Gu, Y.J. & Dziewonski, A.M., 2002. Global variability of transition zone thickness, *J. geophys. Res.*, **107**, doi:10.1029/2001JB000489.
- Gu, Y.J. & Sacchi, M., 2009. Radon transform methods and their applications in mapping mantle reflectivity structure, *Surv. Geophys.*, **30**, 327–354.
- Gu, Y.J., Dziewonski, A.M. & Agee, C.B., 1998. Global de-correlation of the topography of transition zone discontinuities, *Earth planet. Sci. Lett.*, **157**, 57–67.
- Gu, Y.J., Dziewonski, A.M. & Ekström, G., 2003. Simultaneous inversion for mantle shear velocity and topography of transition zone discontinuities, *Geophys. J. Int.*, **154**(2), 559–583.
- Gu, Y.J., Okeler, A. & Schultz, R., 2012. Tracking slabs beneath northwestern Pacific subduction zones, *Earth planet. Sci. Lett.*, **331**, 269–280.
- Gurrola, H. & Rogers, K.D., 2013. New insight into the upper mantle structure beneath the Pacific Ocean using *PP* and *SS* precursors, in *Proceedings of the AGU 2013 Fall Meeting*, abstract #T11C-2460.
- Harlan, W.S., Claerbout, J.F. & Rocca, F., 1984. Signal/noise separation and velocity estimation, *Geophysics*, **49**, 1869–1880.
- Heit, B., Yuan, X., Bianchi, M., Kind, R. & Gossler, J., 2010. Study of the lithospheric and upper-mantle discontinuities beneath eastern Asia by *SS* precursors, *Geophys. J. Int.*, **183**, 252–266.
- Helffrich, G., 2000. Topography of the transition zone seismic discontinuities, *Rev. Geophys.*, **38**(1), 141–158.
- Houser, C., Masters, G., Flanagan, M. & Shearer, P., 2008. Determination and analysis of long-wavelength transition zone structure using *SS* precursors, *Geophys. J. Int.*, **174**, 178–194.
- Houser, C. & Williams, Q., 2010. Reconciling Pacific 410 and 660 km discontinuity topography, transition zone shear velocity patterns, and mantle phase transitions, *Earth planet. Sci. Lett.*, **296**(3), 255–266.
- Ita, J. & Stixrude, L., 1992. Petrology, elasticity and composition of the mantle transition zone, *J. geophys. Res.*, **97**(B5), 6849–6866.
- Ito, E. & Takahashi, E., 1989. Postspinel transformations in the system  $Mg_2SiO_4$ - $Fe_2SiO_4$  and some geophysical implications, *J. geophys. Res.*, **94**, 10 637–10 646.
- Kim, M.J. & Lawrence, J.F., 2013. Global 3D mantle transition zone topography using finite frequency inversion of *SS* precursor travel time, in *Proceedings of the AGU Fall Meeting Abstracts*, Vol. 1, p. 03.
- Laske, G., Masters, G., Ma, Z. & Pasyanos, M., 2013. CRUST1.0: An updated global model of Earth’s crust, in *Proceedings of the EGU General Assembly Conference Abstracts*, Vol. 14, p. 3743.

- Lawrence, J.F. & Shearer, P.M., 2008. Imaging mantle transition zone thickness with *SdS-SS* finite-frequency sensitivity kernels, *Geophys. J. Int.*, **174**, 143–158.
- Ottolini, R., 1983. Signal/noise separation in dip space, Stanford Exploration Project-37, pp. 143–149.
- Ringwood, A.E., 1975. *Composition and Petrology of the Earth's Mantle*, McGraw-Hill.
- Schaeffer, A.J. & Lebedev, S., 2013. Global shear speed structure of the upper mantle and transition zone, *Geophys. J. Int.*, **194**(1), 417–449.
- Schmerr, N., 2012. The Gutenberg discontinuity: melt at the lithosphere-asthenosphere boundary, *Science*, **335**(6075), 1480–1483.
- Schmerr, N. & Garnero, E., 2006. Investigation of upper mantle discontinuity structure beneath the central Pacific using *SS* precursors, *J. geophys. Res.*, **111**, doi:10.1029/2005JB004197.
- Schmerr, N. & Garnero, E., 2007. Upper mantle discontinuity topography from thermal and chemical heterogeneity, *Science*, **318**(5850), 623–626.
- Schmerr, N. & Thomas, C., 2011. Subducted lithosphere beneath the Kuriles from migration of *PP* precursors, *Earth planet. Sci. Lett.*, **311**, 101–111.
- Schmerr, N., Garnero, E. & McNamara, A., 2010. Deep mantle plumes and convective upwelling beneath the Pacific Ocean, *Earth planet. Sci. Lett.*, **294**(1–2), 143–151.
- Schmerr, N., Kelly, B.M. & Thorne, M.S., 2013. Broadband array observations of the 300 km seismic discontinuity, *Geophys. Res. Lett.*, **40**, 1–6.
- Schultz, R. & Gu, Y.J., 2013a. Multiresolution imaging of mantle reflectivity structure using *SS* and *P' P'* precursors, *Geophys. J. Int.*, **195**(1), 668–683.
- Schultz, R. & Gu, Y.J., 2013b. Flexible, inversion-based Matlab implementation of the Radon transform, *Comput. Geosci.*, **52**, 437–442.
- Shearer, P.M., 1991. Constraints on upper mantle discontinuities from observations of long-period reflected and converted phases, *J. geophys. Res.*, **96**, 18 147–18 182.
- Shearer, P.M., 2000. Upper mantle seismic discontinuities, in *Earth's Deep Interior: Mineral Physics and Tomography from the Atomic to the Global Scale*, AGU Geophysical Monograph 117, pp. 115–131.
- Shearer, P.M., Flanagan, M.P. & Hedlin, A.H., 1999. Experiments in migration processing of *SS* precursor data to image upper mantle discontinuity structure, *J. geophys. Res.*, **104**(B4), 7229–7242.
- Shlivinski, A., Heyman, E. & Boag, A., 2005. A pulsed beam summation formulation for short pulse radiation based on windowed Radon transform (WRT) frames, *IEEE Trans. Antenn. Propagat.*, **53**, 3030–3048.
- Stixrude, L., 1997. Structure and sharpness of phase transitions and mantle discontinuities, *J. geophys. Res.*, **102**(B7), 14 835–14 852.
- Thomas, C. & Billen, M.I., 2009. Mantle transition zone structure along a profile in the SW Pacific: thermal and compositional variations, *Geophys. J. Int.*, **176**, 113–125.
- Vacher, P., Mocquet, A. & Sotin, C., 1998. Computations of seismic profiles from mineral physics: the importance of the non-olivine components for explaining the 660 km depth discontinuity, *Phys. Earth planet. Inter.*, **106**, 275–298.
- Ventosa, S. & Romanowicz, B., 2015. Extraction of weak PcP phases using the slant-stacklet transform. Part I: method and examples, *Geophys. J. Int.*, **201**(1), 207–223.
- Ventosa, S., Simon, C. & Schimmel, M., 2012. Window length selection for optimum slowness resolution of the local-slant-stack transform, *Geophysics*, **77**(2), V31–V40.
- Wolfe, C.J., Solomon, S.C., Laske, G., Collins, J.A., Detrick, R.S., Orcutt, J.A., Bercovici, D. & Hauri, E.H., 2009. Mantle shear-wave velocity structure beneath the Hawaiian hot spot, *Science*, **326**, 1388–1390.
- Yu, C., Day, E.A. & van der Hilst, R.D., 2013. Imaging upper mantle discontinuities with *SS* precursors: a comparative study of the generalized radon transform method and the common middle point stacking method, in *Proceedings of the AGU Fall Meeting Abstracts*, Vol. 1, p. 2274.
- Zhao, L. & Chevrot, S., 2003. *SS*-wave sensitivity to upper mantle structure: implications for the mapping of transition zone discontinuity topographies, *Geophys. Res. Lett.*, **30**(11), 1590, doi:10.1029/2003GL017223.
- Zheng, Z. & Romanowicz, B., 2012. Do double '*SS* precursors' mean double discontinuities?, *Geophys. J. Int.*, **191**(3), 1361–1373.